Publ. Astron. Soc. Japan (2021) 73 (6), 1563–1574
https://doi.org/10.1093/pasj/psab098
Advance Access Publication Date: 2021 November 2

Multi-frequency radio observations of the radio-loud magnetar XTE J1810−197

Sujin Eie,[1,2,*] **Toshio Terasawa**,[2] **Takuya Akahori**,[2,3] **Tomoaki Oyama**,[2] **Tomoya Hirota**,[2,4] **Yoshinori Yonekura**,[5] **Teruaki Enoto**,[6] **Mamoru Sekido**,[7] **Kazuhiro Takefuji**,[7,8] **Hiroaki Misawa**,[9] **Fuminori Tsuchiya**,[9] **Shota Kisaka**,[10,11,12] **Takahiro Aoki**,[13] **and Mareki Honma**[1,2,4]

[1]Department of Astronomy, Graduate School of Science, The University of Tokyo, 7-3-1 Hongo, Bunkyo-ku, Tokyo 113-0033, Japan
[2]Mizusawa VLBI Observatory, National Astronomical Observatory of Japan, 2-21-1 Osawa, Mitaka, Tokyo 181-8588, Japan
[3]SKA Organization, Jodrell Bank, Lower Withington, Macclesfield, SK11 9DL, UK
[4]Department of Astronomical Science, The Graduate University for Advanced Studies (SOKENDAI), 2-21-1 Osawa, Mitaka, Tokyo 181-8588, Japan
[5]Center for Astronomy, Ibaraki University, 2-1-1 Bunkyo, Mito, Ibaraki 310-8512, Japan
[6]Extreme Natural Phenomena RIKEN Hakubi Research Team, RIKEN Cluster for Pioneering Research, 2-1 Hirosawa, Wako, Saitama 351-0198, Japan
[7]Kashima Space Technology Center, National Institute of Information and Communications Technology, 893-1 Hirai, Kashima, Ibaraki 314-8501, Japan
[8]Japan Aerospace Exploration Agency, Usuda Deep Space Center, 1831-6 Oomagari, Kamiodagiri, Saku, Nagano 384-0306, Japan
[9]Planetary Plasma and Atmospheric Research Center, Tohoku University, 6-3 Aoba, Aramaki, Aoba-ku, Sendai, Miyagi 980-8578, Japan
[10]Frontier Research Institute for Interdisciplinary Sciences, Tohoku University, Sendai 980-8578, Japan
[11]Astronomical Institute, Tohoku University, 6-3 Aoba, Aramaki, Aoba-ku, Sendai, Miyagi 980-8578, Japan
[12]Department of Physical Science, Hiroshima University, 1-3-1 Kagamiyama, Higashi-Hiroshima, Hiroshima 739-8526, Japan
[13]The Research Institute for Time Studies, Yamaguchi University, 1677-1 Yoshida, Yamaguchi, Yamaguchi 753-8511, Japan

*E-mail sujin.eie@grad.nao.ac.jp

Received 2021 June 29; Accepted 2021 September 22

Abstract

We report on the multi-frequency multi-epoch radio observations of the magnetar XTE J1810−197, which exhibited a radio outburst from 2018 December after its 10-year quiescent period. We performed quasi-simultaneous observations with VERA (22 GHz), Hitachi (6.9 GHz and 8.4 GHz), Kashima (2.3 GHz), and Iitate (0.3 GHz) radio telescopes located in Japan to trace the variability of the magnetar radio pulsations during the observing period from 2018 December 13 to 2019 June 12. The pulse width becomes narrower as the observing frequency goes higher, analogous to the general profile narrowing behavior of ordinary pulsars. When assuming a simple power law in the range of 2.3 GHz

and 8.7 GHz, the radio spectrum of the magnetar goes steeper with the average spectral index $\langle\alpha\rangle \approx -0.85$ for the first four months. The wide-band radio spectra gathered from our observations and the literature suggest that XTE J1810−197 would have a double-peaked spectrum with a valley point in 22–150 GHz, where the first spectral peak implies a gigahertz-peaked spectrum (GPS) feature with a peak at a few GHz. The GPS and the high-frequency peak have been identified in the spectra of other radio-loud magnetars, thus they may be intrinsic features that can give a new insight to the understanding of various emission mechanisms and the surrounding environments of radio magnetars. Our study emphasizes the importance of simultaneous long-term broad-band observations toward radio-loud magnetars to capture the puzzling spectral features and establish a link to other types of neutron stars.

Key words: pulsars: general — pulsars: individual (XTE J1810−197) — stars: magnetars

1 Introduction

Magnetars, which are a subset of pulsars with strong X-ray/γ-ray outbursts, have long rotation periods (>1 s) and large spin-down rates, suggesting that they are young ($\lesssim 10^4$ yr) neutron stars with extremely strong magnetic fields ($\geq 10^{14}$ G) (Thompson & Duncan 1993). While radio pulsation is a common nature of ordinary pulsars, only six out of ∼30 confirmed magnetars have shown detectable radio pulses as of 2020 November (Olausen & Kaspi 2014).[1] The radio pulses from magnetars have some properties that are different from those of ordinary pulsars.

One different property is the radio frequency spectrum; the spectral index, α, defined with the total intensity I and the frequency ν as $I \propto \nu^{\alpha}$, is close to zero (e.g., Torne et al. 2015) and a gradual spectral steepening has been seen in some cases (e.g., Lazaridis et al. 2008), while ordinary pulsars show much steeper spectra with the average spectral index $\langle\alpha\rangle = -1.8 \pm 0.2$ (Maron et al. 2000). The flatter spectra of radio-loud magnetars lead to relatively stronger radio emission at high frequencies. This allows us to explore the new type of neutron star emission in much wider radio bands.

Another different property is the strong time-variability of flux density, spectrum, pulse shape, and polarization (e.g., Camilo et al. 2008; Lazaridis et al. 2008; Levin et al. 2010). The variation trend is poorly understood, nevertheless the fluctuations are known to be extreme in both the short and long term. Even their radio emissions are transient phenomena; their appearance is possibly associated with X-ray outbursts (e.g., Anderson et al. 2012). The flatter spectra and erratic variations of magnetar radio pulsations have been thought to be intrinsic to magnetars themselves, suggesting a possibility that there are some different radio-emission mechanisms in neutron star magnetospheres.

[1] McGill Online Magnetar Catalog ⟨http://www.physics.mcgill.ca/~pulsar/magnetar/main.html⟩.

The triggers for these extraordinary features are not yet figured out, despite numerous hypotheses on the origins of magnetars. Meanwhile, Camilo et al. (2016) suggested that the spectrum of XTE J1810−197 became steeper down to $\alpha \approx -3$ before it entered the radio-quiescent period. Such a steep spectrum at a late phase of outburst looks like, or is even steeper than, that of ordinary pulsars, which can imply a possible similarity in emission mechanism except that the magnetar pulsations faded out as a result of unknown reasons. Very recently, in addition, the discovery of a fifth radio-loud source showed that the magnetar Swift J1818.0−1607 has a steep spectrum with $\alpha \simeq -2.26$ (Lower et al. 2020) even soon after the radio outburst emerged. This opened the new paradigm that a magnetar can also emit radio pulses akin to those from ordinary pulsars. Its spectrum later flattened (Majid et al. 2020), implying the variety of magnetar spectral changes. Because such behavior is known in only one example to data, it is important to examine spectral indices and time variability for other magnetar radio outbursts.

XTE J1810−197 is known as the first radio-loud magnetar (Halpern et al. 2005) as well as the first transient magnetar detected with a significant increase of its X-ray luminosity (Ibrahim et al. 2004). The rotational period, $P = 5.541$ s, and the spin-down rate, $\dot{P} = 2.83 \times 10^{-11}$ s s^{-1} (Pintore et al. 2016), imply the strength of the dipole magnetic field, $B_{\rm d} = 3.2 \times 10^{19}\sqrt{P\dot{P}} \approx 1.3 \times 10^{14}$ G, and the characteristic age, $\tau_{\rm c} = P/2\dot{P} \approx 31000$ yr, both of which are typical values for magnetars. Radio pulsations of XTE J1810−197 were detected in 2006 with the very same period of X-ray pulsations (Camilo et al. 2006). After that, the radio flux density dramatically decreased. Then, it turned out to be in a quiescent state from 2008 November (Camilo et al. 2016). Hereafter, we call the radio-bright period in 2005–2008 "the previous outburst."

After the long radio-silent phase of about 10 years, intense radio pulses from XTE J1810−197 were again

observed on MJD 58460 (2018 December 8) (Lyne et al. 2018). Gotthelf et al. (2019) reported an earlier increase of its X-ray flux between MJDs 58442 and 58448, and confirmed that an X-ray outburst had preceded the radio burst. Many radio follow-up observations have reported a broad frequency range in its radio activity during this outburst, from 300 MHz (Maan et al. 2019) to a few GHz (Levin et al. 2019; Dai et al. 2019; Johnston et al. 2020), to 32 GHz (Pearlman et al. 2019) and even up to 150 GHz and 260 GHz (Torne et al. 2020).

These extensive studies of XTE J1810−197 at multiple radio frequencies during the second outburst, however, mostly cover time spans shorter than two months and are less overlapped in the observing periods. This could restrict the comprehensive understanding of highly variable magnetar emission in frequency and time domains. Simultaneous broad radio-band observations of radio magnetars over a wide time span that can capture data from the very first moment of an outburst would enable observers to trace their long-term emission evolution and gather the low- and high-frequency characteristics at the same time, providing important aspects for understanding the behavior of one of the early phases of neutron stars.

In this paper, we analyze our radio data of $\sim$ monthly observations of XTE J1810−197 during its second outburst and investigate the temporal and frequency evolutions of its pulsed emission for six months. This paper is organized as follows. In section 2, we describe our observations and data reduction. We show the variations in spin parameters, pulse profile, flux, and spectrum in section 3. In section 4, we discuss our results of the spectra and pulse widths and underline the significance of simultaneous long-term broad-band observations of radio magnetars.

2 Observation and data reduction

We have conducted roughly-monthly, quasi-simultaneous, single-dish observations using radio telescopes in Japan. The observations started on MJD 58465 (2018 December 13), five days after the first report of the strong radio flares of XTE J1810−197 in late 2018 (Lyne et al. 2018). Our observations were organized at 0.3 GHz, 2.3 GHz, 6.9 GHz, 8.4 GHz, and 22 GHz, and they are summarized in table 1. If the time difference between observations is shorter than $\sim$ a day, we classified them as being in the same session, assuming that the averaged pulse shape would not change significantly over 24 hours.

2.1 Observations

VERA (VLBI Exploration of Radio Astrometry) is a very long baseline interferometry (VLBI) array operated by the National Astronomical Observatory of Japan (NAOJ) (VERA Collaboration 2020). VERA consists of four 20 m diameter antennas located at Mizusawa, Iriki, Ishigaki, and Ogasawara in Japan. The director's discretionary time observations of XTE J1810−197 with VERA were conducted for four sessions, and the total amount of observing time per session is $\sim$4.2 hr including overhead. We note that VLBI was not achieved owing to a lack of a bright calibrator. In this study, therefore, we utilized the four VERA stations as four separate single-dish telescopes. Among them, Ishigaki station did not capture any pulsed signals which were observed at the other three VERA stations. This is likely due to bad weather at that station; we therefore exclude the data of Ishigaki station from our data reduction for this study. For the remaining stations, the *K*-band (21.5–23.5 GHz) receiver was used and the left-hand circular polarized (LCP) waves were recorded. The 22 GHz data of VERA was recorded after divided into four sub-bands (bandwidth of 512 MHz each) with a data recording rate of 2048 Mbps. Due to the weak intensity of the magnetar, we integrated the four sub-bands into one broad-band in order to increase the continuum sensitivity by a factor of 2. We then combined the three VERA stations into one dataset to earn an additional increase of the sensitivity (a factor of $\sqrt{3}$) after the phase is aligned by the barycentric dynamical time (TDB).

The Hitachi 32 m telescope is located at Hitachi in Japan (Yonekura et al. 2016). Operated by Ibaraki University, Hitachi observations were performed for nine sessions. The C-band (6.6–7.1 GHz) and X-band (8.1–8.7 GHz) receivers recorded LCP and right-hand circular polarized (RCP) waves, respectively. Each band has the bandwidth of 512 MHz and the data recording rate of 2048 Mbps.

The Kashima 34 m telescope had been operated by the National Institute of Information and Communications Technology (NICT) of Japan. The telescope was located at Kashima, Japan. We used the S-band (2210–2350 MHz) receiver and recorded RCP waves. It is found that the second sub-band among four-divided frequency bands (bandwidth of 32 MHz each) of Kashima data is highly contaminated by radio frequency interferences (RFIs), hence 96 MHz in the recorded bandwidth was chosen for our analysis.

IPRT (Iitate Planetary Radio Telescope) is a dual symmetric offset parabolic antenna with an aperture size of 31 m $\times$ 16.5 m in two sets (aperture area of 1023 m^2 in total; Iwai et al. 2012). The telescope is located at Iitate, Japan, and operated by Tohoku University, primarily for investigating the dynamic behavior of Jupiter's synchrotron radiation (Tsuchiya et al. 2010) and solar radio emission at low frequencies. It has also been used for the study of giant pulses from the Crab pulsar (Mikami et al. 2016). We

Table 1. Summary of observations.*

(1)	Date (MJD) (2)	$\nu_{\rm center}$ (BW) [MHz] (3)	Pol. (4)	SEFD [Jy] (5)	$t_{\rm start}$ [hh:mm] (6)	$t_{\rm obs}$ [hr] (7)	(8)
1	2018 December 13	6856 (512)	L	157.8	23:30	1.5	Y
	(58465)	8448 (512)	R	137.4	23:30	1.5	Y
	2018 December 14	325.1 (4)	XY	846.0	00:11	2.8	N
	(58466)	2258 (96)	R	532.0	00:10	4.0	Y
2	2018 December 18	6856 (512)	L	139.1	02:00	4.0	Y
	(58470)	8448 (512)	R	122.3	02:00	4.0	Y
		22483 (2048)	L	2944.4	02:44	4.2	Y
3	2019 January 07	325.1 (4)	XY	846.0	01:00	2.0	N
	(58490)	2258 (96)	R	532.0	00:00	0.5	Y
		6856 (512)	L	136.8	01:00	4.2	Y
		8448 (512)	R	123.8	01:00	4.2	Y
		22483 (2048)	L	2820.5	01:24	4.2	Y
4	2019 January 09	6856 (512)	L	137.8	22:40	0.6	Y
	(58492)	8448 (512)	R	129.0	22:40	1.3	Y
5	2019 January 21	22483 (2048)	L	2510.0	00:24	4.2	N
	(58504)						
6	2019 February 15	6856 (512)	L	133.4	21:00	3.0	Y
	(58529)	8448 (512)	R	144.9	21:00	3.0	Y
		22483 (2048)	L	4413.4	21:29	4.2	Y†
7	2019 March 04	2258 (96)	R	532.0	22:00	1.0	Y
	(58546)	6856 (512)	L	136.4	20:00	4.0	Y
		8448 (512)	R	129.2	19:00	5.0	Y
8	2019 March 31	6856 (512)	L	133.2	18:00	4.0	Y
	(58573)	8448 (512)	R	131.1	18:00	4.0	Y
9	2019 April 23	6856 (512)	L	139.2	16:00	4.0	Y
	(58596)	8448 (512)	R	131.1	16:00	4.0	Y
	2019 April 24	325.1 (4)	XY	846.0	16:00	3.6	N
	(58597)	2258 (96)	R	532.0	16:00	4.0	Y
10	2019 June 12	325.1 (4)	XY	846.0	13:00	2.0	N
	(58646)	2258 (96)	R	532.0	13:30	4.0	N
		6856 (512)	L	139.2	13:00	4.0	Y
		8448 (512)	R	131.1	13:00	4.0	Y

*(1) Observing sessions. If observation dates are within a day of one another, we consider those datasets as the same session. (2) UTC-based date and MJD. (3) Center frequency and (in parentheses) effective bandwidth. (4) Polarization information. XY: Cartesian orthogonal, R: RCP, L: LCP. (5) System equivalent flux density (SEFD). (6) Start time of the observation in UT. (7) Total observation time. (8) Detection (Y) or non-detection (N) of the pulsed emission.
†Only six single pulses were detected and an integrated profile was not obtained (see subsection 3.3 for details).

conducted IPRT observations of XTE J1810−197 in the *P* band (323.1–327.1 MHz) and recorded two orthogonal polarized waves.

2.2 Data reduction

The data obtained at frequencies lower than 6.9 GHz were coherently de-dispersed (Hankins & Rickett 1975; Lorimer & Kramer 2012) with the known dispersion measure (DM) of 178 pc cm^{-3} (Camilo et al. 2006) to correct the dispersion delay caused by free electrons in the interstellar medium. Later, each piece of data was averaged in each 2 ms. The frequencies of 8.4 GHz and 22 GHz are high enough to be free from dispersion effects (see also Torne et al. 2015); with the known DM and the given bandwidth, the dispersion delays are 1.3 ms and 0.2 ms at 8.4 GHz and 22 GHz, respectively, which are smaller than the averaging time. Hence, we did not carry out a de-dispersion process on the data at the two frequencies and averaged data for each 2 ms.

Non-periodical RFIs were manually removed from the data in frequency and time domains to prevent any artifacts from being recognized as strong pulses. A general trend caused by atmospheric changes and/or receiver characteristics is also examined and calibrated. The pulsar-timing package `TEMPO2` (Hobbs et al. 2006) is used for transforming the reference frame from each geographic location to the solar system barycenter, i.e., from the coordinated universal time (UTC) to TDB.

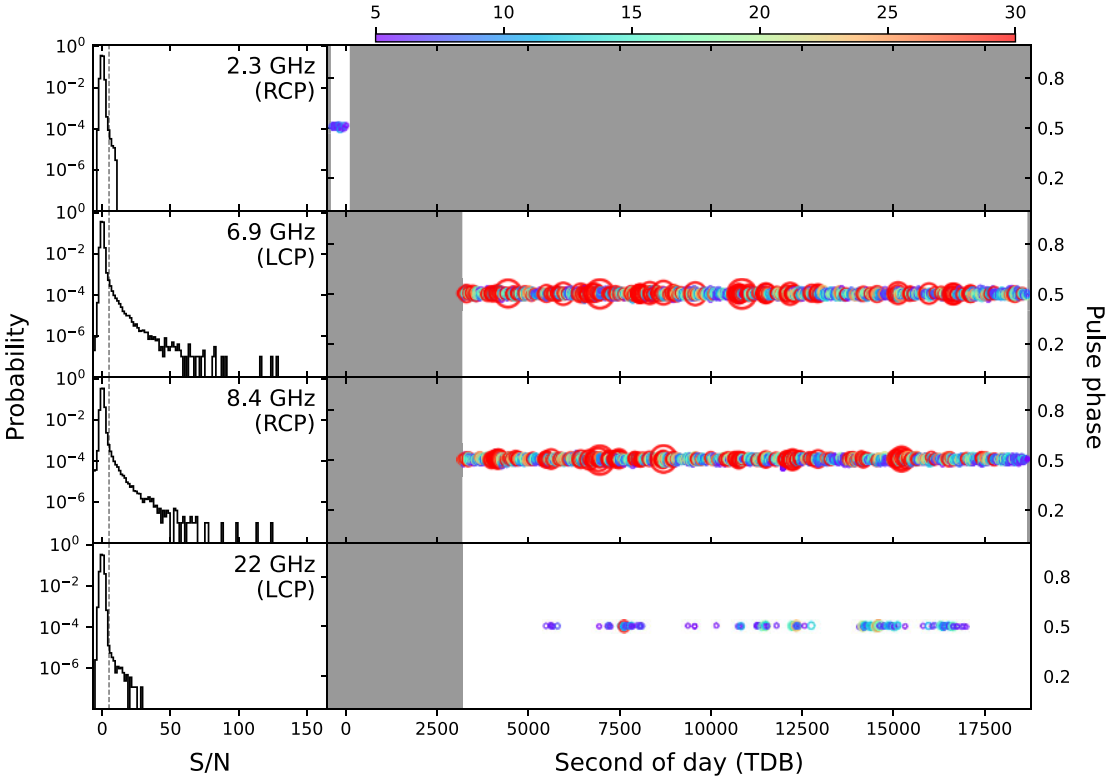

Fig. 1. Left-hand panels: Probability distributions of the S/N of single-pulse components on MJD 58490 (2019 January 7) after RFI cleaning. The vertical dashed line indicates the S/N value of 5, the plotting threshold for the right-hand panels. Right-hand panels: Single pulses detected during our observations on the same date after RFI-cleaning in the time-phase domain. The optimal period and period derivatives on this observing epoch are deduced by the timing solution reported by Levin et al. (2019) (see subsection 3.1 for details), and the phase of the main peak is adjusted to be 0.5 based on the integrated profile at 6.9 GHz. Only signals with $S/N > 5$ are plotted and S/N values are indicated with the size and color scale shown by the color bar on the panels. The gray-shaded areas indicate the time before and after the observations at each band. The Kashima observation at 2.3 GHz was contaminated by strong RFIs ∼106 s after the observation started.

3 Analysis and results

We detected strong pulsed emission from XTE J1810−197 including a number of single pulses in most of our observing sessions in the 2.3–22 GHz bands. We could not detect any pulsed emission at 0.3 GHz over 5σ. The 3σ upper limit on the mean flux density at 0.3 GHz is ∼13 mJy when assuming a duty cycle of 5% (see subsection 3.2 for the assumed duty cycle). We show one sample of the dataset of MJD 58490 in figure 1. No presence of an interpulse is observed during our observations (see also Dai et al. 2019), whereas during the previous outburst in 2006 highly variable interpulse components were intermittently detected at 0.72 of the pulse phase later than the main pulse phase, and some of these were brighter than the main pulses (Kramer et al. 2007; Lazaridis et al. 2008).

3.1 Spin parameters

Levin et al. (2019) determined spin parameters from their nearly-daily observations of XTE J1810−197 in the interval between MJDs 58460 and 58507, which includes our observing sessions 1–5. Single pulses obtained in these sessions are well aligned in phase with their timing results (figure 1). To follow up the timing parameters covering the whole observation period in this work, we determine spin parameters using arrival times of single-pulse components at 8.4 GHz obtained by the Hitachi telescope, except for session 5 when the Hitachi observation was not conducted. The determination process of spin frequency $\nu(t_i)$ (i = 1–9) for session number i is in four steps. (i) We roughly find the optimal spin frequency, $\nu(t_i)$, that derives the maximum signal-to-noise ratio (S/N) in an integrated profile. (ii) Grounded on the $\nu(t_i)$ estimated in the previous step, we search the frequency on closer inspection by conducting weighted least-squares fitting to best align all single pulse components with $S/N > 6$ at the same pulse phase throughout an observation, as seen in figure 1. This gives results consistent with Levin et al. (2019) for the first four sessions. (iii) We fit a Taylor polynomial (making use of the polynomial package `NumPy`),

$$\nu(t_i) = \nu_0 + \dot{\nu}_0(t_i - t_0) + \frac{1}{2}\ddot{\nu}_0(t_i - t_0)^2 + \frac{1}{6}\dddot{\nu}_0(t_i - t_0)^3, \quad (1)$$

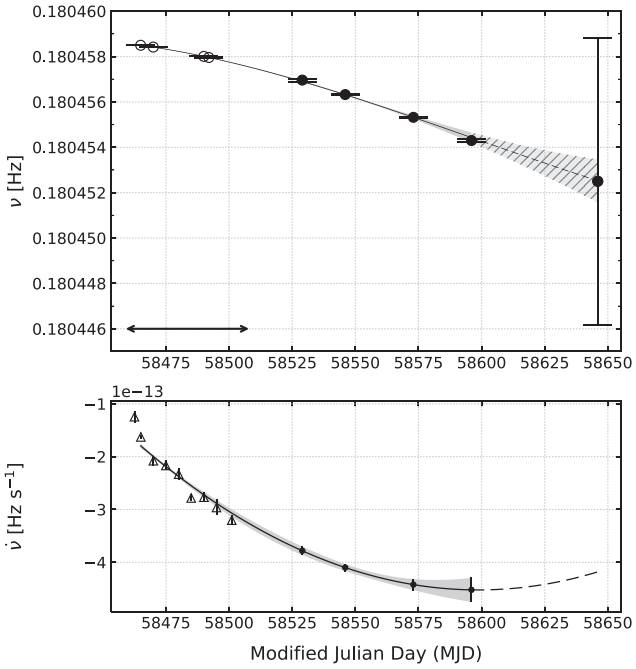

Fig. 2. Top panel: Spin frequencies (ν) of XTE J1810−197 during our observations. The arrow at the bottom left-hand corner indicates the duration of 48 days when pulsar timing solutions were achieved by Levin et al. (2019), i.e., MJDs 58470–58507. Open circles are spin frequencies of our observing sessions 1–4, which are derived by equation (1) with the spin parameters of Levin et al. (2019). Filled circles are the values estimated from our data (see subsection 3.1 for the method). The curved line is a fitted variation of the rotation frequency (solid line: interpolation for MJDs 58507–58596, dashed line: extrapolation of our fit to MJD 58646), and the shaded region encompasses the 3σ confidence interval. Bottom panel: Changes of the spin frequency derivative ($\dot{\nu}$) during our observing period. The solid line indicates $\dot{\nu}$ estimated from the upper panel, and the dashed line is an extrapolation of our fit to MJD 58646 which is excluded from the iteration process (see text for details). The shaded region encompasses 3σ confidence interval. The triangles are data taken from figure 6 in Levin et al. (2019), while black dots indicate the estimated $\dot{\nu}$ of our observing sessions 6–9.

to $\nu(t_i)$ ($i = 1$–9), and estimate derivatives of spin frequency for sessions 6–9. Here we remark that $\nu(t_i)$ ($i = 1$–4; session 5 has non-detection) is obtained from table 1 of Levin et al. (2019) which is derived from observations with a much higher cadence than ours. (iv) Applying the derivatives, we perform step (ii) again by aligning single pulse components in the phase domain. Repeating steps (iii) and (iv) iteratively, we obtain $\nu(t_i)$ ($i = 6$–9) and its derivatives. The last Hitachi observation in session 10 (MJD 58646; 2019 June 12) detected only a few weak single pulses at $>5\sigma$, therefore it is excluded from the above iteration process; i.e., only step (i) was conducted for it, resulting in a large uncertainty of $\nu(t_{10})$. The upper panel of figure 2 shows the resultant $\nu(t_i)$ ($i = 6$–10). The coefficients of the Taylor expansion [equation (1)] are listed in the second row of table 2.

To verify the spin parameters obtained with the data at 8.4 GHz, we applied those parameters to the data at 6.9 GHz and confirmed that the single-pulse components at 6.9 GHz were well aligned in the phase domain. Later we additionally verified that timing with `TEMPO2` gives consistent parameters with our method stated above.

By differentiating equation (1) with respect to t_i, we obtain the spin frequency derivative, $\dot{\nu}$, of the magnetar (figure 2, lower panel). Its absolute value $|\dot{\nu}|$ increased continuously, but the change became more gradual over time by MJD 58596, as was the case during the early 48 days reported by Levin et al. (2019). The similar trend in the X-ray band was also recently reported by Borghese et al. (2021).

3.2 Pulse profiles

Figure 3 shows some examples of single pulse profiles (solid black lines) simultaneously observed at three different frequencies (6.9 GHz, 8.4 GHz, and 22 GHz). We note again that 6.9 GHz and 22 GHz indicate LCP waves, while 8.4 GHz does the same for RCP waves. The shapes of the profiles are highly variable depending on time and polarization. Single pulses are approximately normally distributed within the pulse width, centered at the peak of the average profiles. We confirm that there is no periodicity in their occurrence in time and phase domains. We find that the profiles at 6.9 GHz and 8.4 GHz consist of more multiple components than those at 22 GHz. However, it is possible that the corresponding microstructures at a higher frequency have smaller relative strength such that they are easily shrouded in strong noise. Some distinct

Table 2. Spin parameters of XTE J1810−197 estimated by Levin et al. (2019) and this work.*

Date range [MJD]	Epoch [MJD]	ν_0 [Hz]	$\dot{\nu}_0$ [Hz s^{-1}]	$\ddot{\nu}_0$ [Hz s^{-2}]	$\dddot{\nu}_0$ [Hz s^{-3}]	$\ddddot{\nu}_0$ [Hz s^{-4}]	RMSE [period]
			— Levin et al. (2019) —				
58460–58507	58484.0	0.180458147(2)	$-2.575(4) \times 10^{-13}$	$-5.5(4) \times 10^{-20}$	$-1.7(2) \times 10^{-26}$	$4.2(10) \times 10^{-32}$	0.0007
			— This work —				
58465–58597	58484.0	0.180458142(1)	$-2.52(1) \times 10^{-13}$	$-4.1(2) \times 10^{-20}$	$4.1(11) \times 10^{-27}$	—	0.15

*Numbers in parenthesis represent 1σ errors in unit of the last significant digits.

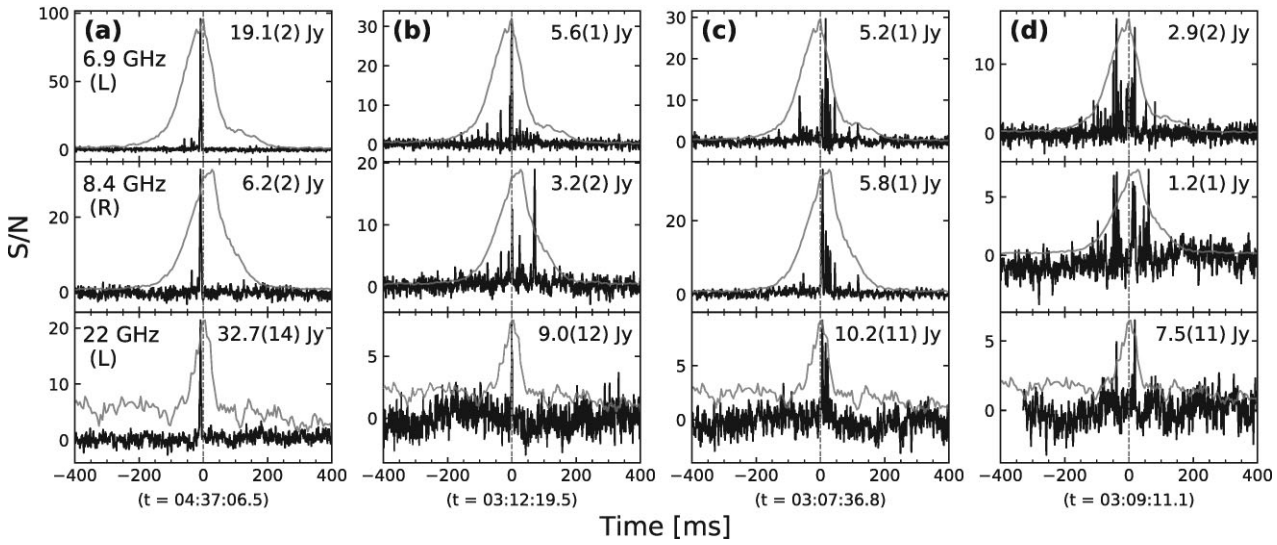

Fig. 3. Four examples of single pulses detected simultaneously at 6.9 (LCP), 8.4 (RCP), and 22 GHz (LCP) on MJD 58490 (2019 January 7). They are listed in order of complexity from left to right. The horizontal axes are aligned in TDB and set to zero at the peak phase of the average profile at 6.9 GHz, as in figure 1. The vertical dashed lines indicate the central phase of 0.5. The peak flux density of each single pulse profile is marked in the Jansky level, where its 1σ error in the last digit is shown in parentheses. The average profiles at the same frequency on MJD 58490 are shown as the solid gray lines, and scaled to the peak S/N in each panel.

Table 3. Profile widths at 10% ($W10_{\rm MJD}$) and 50% ($W50_{\rm MJD}$) of the peak intensity at each circular polarization and observing frequency.*

Pol.	Observing frequency	$W10_{58465}$ [%]	$W10_{58470}$ [%]	$W10_{58490}$ [%]	$W10_{58492}$ [%]	$W10_{58529}$ [%]	$W10_{58546}$ [%]	$W10_{58573}$ [%]	$W10_{58596}$ [%]	$W10_{58646}$ [%]
RCP	2.3 GHz	5.7		—			—		—	—
	8.4 GHz	3.8	4.3	4.9	4.6	—	4.6	3.2	—	—
LCP	6.9 GHz	5.7	4.7	4.9	4.1	5.4	4.7	—	—	—
	22 GHz		4.2	2.4		—				
Pol.	Observing frequency	$W50_{58465}$ [%]	$W50_{58470}$ [%]	$W50_{58490}$ [%]	$W50_{58492}$ [%]	$W50_{58529}$ [%]	$W50_{58546}$ [%]	$W50_{58573}$ [%]	$W50_{58596}$ [%]	$W50_{58646}$ [%]
RCP	2.3 GHz	3.0		2.4			2.5		1.1	—
	8.4 GHz	1.8	1.6	2.1	2.2	2.1	2.3	2.0	2.5	2.7
LCP	6.9 GHz	3.7	3.0	1.9	2.1	2.3	1.9	2.2	2.7	
	22 GHz		1.4	0.9		—				

*Pulse widths $W10_{\rm MJD}$ and $W50_{\rm MJD}$ are given in percentage of the duty cycle. Entries of "—" indicate that an observation was conducted but the width is less than the 3σ confidence.

examples of the multiplicity are shown in panels (c) and (d) of figure 3. In addition, strong pulse-to-pulse profile variations are prominently seen in figure 3 when considering the direction of circular polarization. We could not discern if the variations are due to the change of the intensity of circular polarization or the real change of total intensity.

The average profiles are overlaid in figure 3 with solid gray lines. It is clear that single pulses have much narrower widths compared to the corresponding average profile. The pulse width is measured as the width at 10% of the maximum intensity (W_{10}) of an integrated profile when 10% of the intensity is greater than 3σ (table 3). This derives a duty cycle of $\sim$5% in the 2.3–8.4 GHz range, which is comparable to the duty cycle during the previous outburst of XTE J1810−197 (Camilo et al. 2016) as well as to the typical duty cycle of ordinary pulsars (Maciesiak et al. 2011). Since 10% of the maximum intensity of the profiles at 22 GHz is less than 3σ, we measure the widths at 50% of the peak intensity (W_{50}) and compare it with W_{50} at other frequencies in the same session. For each direction of the circular polarization, the pulse width W_{50} (duty cycle, likewise) becomes slightly narrower as the observing frequency goes higher.

The average profile at 8.4 GHz is delayed when compared to those at 6.9 GHz and 22 GHz (see the phases at the peaks of solid gray profiles in figure 3). The degree of

Table 4. Conversion factors between the intensity at a single circular polarization and the total intensity.*

ν_{center} [MHz]	MJD 58463 (2018 Dec. 11)		MJD 58467 (2018 Dec. 15)		MJD 58470 (2018 Dec. 18)	
	I/L	I/R	I/L	I/R	I/L	I/R
1024	1.97	2.03	2.29	1.77	2.06	1.94
1920	1.55	2.81	2.16	1.86	2.45	1.69
2816	1.69	2.44	2.03	1.97	2.25	1.80
3712	1.79	2.27	2.07	1.93	2.54	1.65

*I indicates the total intensity, L the intensity at LCP, and R the intensity at RCP. The values are estimated from the averaged polarization pulse profiles by Dai et al. (2019) (see subsection 3.3 for details).

the phase delay is different at different observing epochs, but larger in earlier sessions. We presumed that the phase shift is caused by the time variations of the polarization degree, then we compared it with the polarization profiles of XTE J1810−197 in the literature. Taking into account a polarization study during MJDs 58463–58470 at 0.7–4 GHz (Dai et al. 2019), we derived LCP and RCP profiles from the total intensity (I) and circular polarization (V) profiles as $I(\mathrm{LCP}) = (I + V)/2$ and $I(\mathrm{RCP}) = (I - V)/2$. The degree of the phase shift between our profiles at 6.9 and 22 GHz (LCP) and 8.4 GHz (RCP) on MJD 58470 (2018 December 18) is comparable with that between the two profiles at different circular polarization handedness taken from Dai et al. (2019) on MJD 58470. We, therefore, suggest the phase delay of averaged profiles shown in figure 3 would be on account of the different polarization degrees in each session.

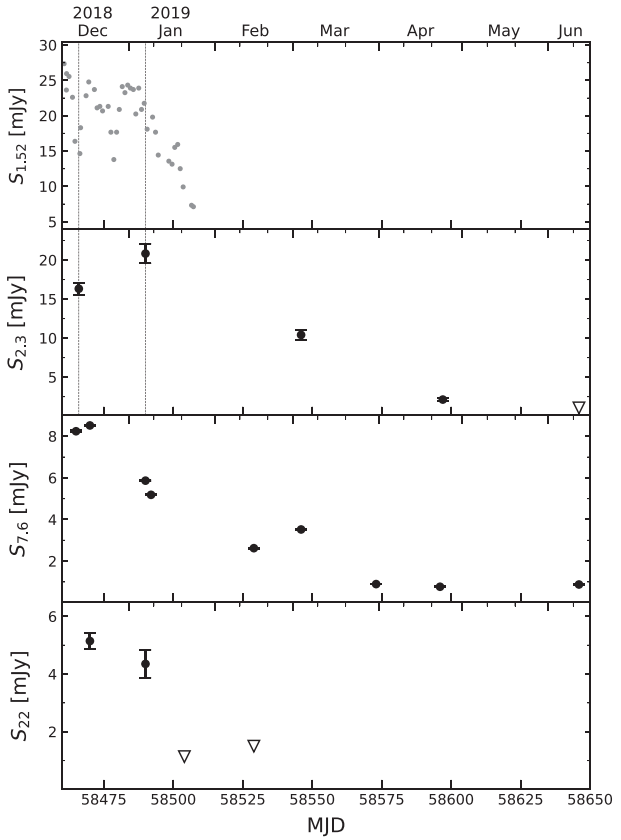

Fig. 4. Top panel: Daily flux density variations at 1.52 GHz ($S_{1.52}$). Data are from Levin et al. (2019). Lower panels: Variations of total intensity of XTE J1810−197 at 2.3 GHz, 7.6 GHz, and 22 GHz ($S_{2.3}$, $S_{7.6}$ and S_{22}, respectively). Dashed vertical lines indicate the first session at 2.3 GHz, when the 1.52 GHz brightness has drastically decreased (first local minimum), and the second session, when the brightness is recovered from the next local minimum. Triangles indicate the upper limits.

3.3 Flux variations

To discuss the flux variations of XTE J1810−197, we estimate the total intensity, I, from single circular polarizations, LCP and RCP, as follows. In the case of the data simultaneously taken with Hitachi (LCP at 6.9 GHz and RCP at 8.4 GHz), we simply combine them in each time bin (TDB) as $I = I(\mathrm{LCP}) + I(\mathrm{RCP})$ at 7.6 ± 1.1 GHz. For the other data (Kashima 2.3 GHz and VERA 22 GHz), we measure conversion factors for converting the intensity at one circular handedness to the total intensity. From the RCP and LCP profiles derived from the data obtained by Dai et al. (2019), as described in subsection 3.2, we calculate the ratio of mean flux densities of RCP or LCP profiles to the total flux density. Reciprocals of the ratios, I/LCP or I/RCP, are shown in table 4. We employ these conversion factors to derive the total intensities at 2.3 GHz and 22 GHz. Although the conversion factors can depend on the frequency, there is no significant change in the polarization profiles between 1920.0 and 3712.0 MHz (Dai et al. 2019). Therefore, we assume the polarization property at 3712.0 MHz would be stable up to 22 GHz, and apply the conversion factors obtained at 3712 MHz on MJD 58470 (2018 December 18) to our data at 22 GHz obtained on the same date. Additionally, the integrated profiles at 7.6 GHz do not appear to undergo significant temporal evolution during our observing period, thus we suppose that the averaged polarization pulse profiles and the averaged polarization angle are both relatively stable during this outburst. Therefore, we assume that the conversion factors do not significantly change during our observing period, and apply the mean conversion factors (2.07 ± 0.08 and 2.01 ± 0.09 for LCP and RCP, respectively) to the other data excepting that from MJD 58470.

As a result, figure 4 shows time variations of total intensity at 2.3 GHz, 7.6 GHz, and 22 GHz. To compare and understand the variations with those at a lower frequency, daily flux densities at 1.52 GHz (data from Levin et al. 2019) are marked in the top panel of figure 4.

Mean flux density at 2.3 GHz was higher on MJD 58490 (2019 January 7) than that on MJD 58466 (2018 December

14). We note that this does not necessarily mean the intensity has gradually increased for a month; Levin et al. (2019) showed two drastic decreases in daily flux at 1.52 GHz within a month during this outburst, and MJD 58466 is when the flux was in the first trough. Meanwhile, MJD 58490 is after the 1.52 GHz intensity recovered from the second trough (see vertical dashed lines in figure 4). Therefore, we remark that the early change at 2.3 GHz reflects erratic daily changes which are seen at the lower frequency. The last 2.3 GHz observation on MJD 58646 (2019 June 12) did not capture any pulsed emission and gives only an upper limit, as marked with a triangle in figure 4.

On the other hand, the flux density at 7.6 GHz does not seem to follow the low-frequency behavior fully on the same dates. In session 3 (MJD 58490; 2019 January 7), the intensity at 7.6 GHz is not brighter than the previous sessions, unlike the similar flux changes between 1.52 and 2.3 GHz. The time-variable spectral indices are rather common for radio magnetars (e.g., Anderson et al. 2012; Pennucci et al. 2015; Champion et al. 2020), thus this would reflect a typical behavior of magnetar radio emission. Otherwise, this may suggest that there is a time lag in daily variations between low and high frequencies or that the flux variation includes narrow-band behaviors, which are not easily studied due to the strong variability.

Among four 22 GHz observations, we obtained integrated profiles only during the first and second sessions. We found that the third session is when the luminosity at 1.52 GHz is two times fainter than in the second session (Levin et al. 2019), which may imply the general flux variations would be the wide-band feature. On MJD 58529 (2019 February 15) at 22 GHz, we found only six single pulses at $>6\sigma$ significance, due to the relatively low sensitivity. We thus marginally obtained the integrated pulse profile, hence no confident mean flux density is measured. The detection of a few re-occurring strong single pulses manifests the huge variability in flux density up to high frequencies.

While the long-term variation of flux density might have been affected by daily variations, we see that the radio intensity generally gets fainter over time. This result is in agreement with previous studies (e.g., Camilo et al. 2007a). During the previous radio outburst of XTE J1810−197 in 2005–2008, Camilo et al. (2016) reported that it showed a significant decrease in the mean flux density at 1.4–3 GHz, to a factor of 20 fainter than the first measured pulsed intensity during the first 10 months, followed by a stable period for a twice-longer period until it paused the radio emission. From our higher-frequency observations, however, the intensity became ∼10 times fainter at 7.6 GHz in the six months after the outburst, therefore it may not suggest a clear manifestation of radio cessation but imply a continuously decreasing phase in 2019 June. Considering that the first radio detection in 2005 of XTE J1810−197 was half a year later than its X-ray outburst and an additional year passed until the first detection of radio pulses, we estimate the time range of the observable decreasing phase in intensity would be longer for this outburst if the radio turn-off mechanism is analogous to its previous radio outburst. Further monitoring observations until this radio outburst comes to the end, therefore, are needed to compare the radio behaviors and physical properties of XTE J1810−197 between the two outbursts.

3.4 Spectral variations

We present the spectra of XTE J1810−197 between 2.3 and 22 GHz obtained (quasi-) simultaneously. The time gaps between observations are smaller than 24 hours, if not simultaneous. Figure 5 shows five spectra between 2018 December and 2019 April, with early results of precedent studies (Maan et al. 2019; Dai et al. 2019; Pearlman et al. 2019, 2020; Torne et al. 2020). Our upper limit at 0.3 GHz is marked as well.

Even though each data point could be affected by short-term (shorter than a day) variations in flux density, our results suggest clear negative spectral indices in centimeter-wavelengths. The daily variations shown in figure 4 lead to the high variability in spectral indices, though we found the spectrum in 2.3–8.7 GHz becomes steeper during the period when assuming a power law; $\alpha = -0.57 \pm 0.04$ on MJD 58465 to -0.85 ± 0.10 on MJD 58596. During the previous outburst in 2006, the spectral index of the main pulse also became steeper from 0.05 ± 1.12 (MJD 53873) to -0.90 ± 0.38 (MJD 53983) in the frequency range of 1.4–4.9 GHz during the first ∼ four months (Camilo et al. 2007b). Therefore, XTE J1810−197 shows a faster decline in its intensity towards higher frequency, both in the previous outburst and this one.

The mean power-law spectral index in 2.3–8.7 GHz during the 4.5 months of our observations is $\langle\alpha\rangle = -0.85 \pm 0.14$. With regard to the spectrum up to 8 GHz, the previously measured index on MJD 53862 (2006 May 7) is -0.30 ± 0.04 between 1.4 and 8.5 GHz (Camilo et al. 2007b), implying that the decreasing trends of the flux density at the radio frequency higher than 4 GHz are both observed in the previous outburst and this radio outburst.

4 Discussion

4.1 Double-peaked spectrum?

In figure 5, we overlay the flux densities obtained by Dai et al. 2019 (0.7–4 GHz), Maan et al. 2019 (0.3–0.7 GHz), Pearlman et al. 2019 (8.4 and 32 GHz), Pearlman et al. 2020 (8.3 and 31.9 GHz), and Torne et al. 2020 (150

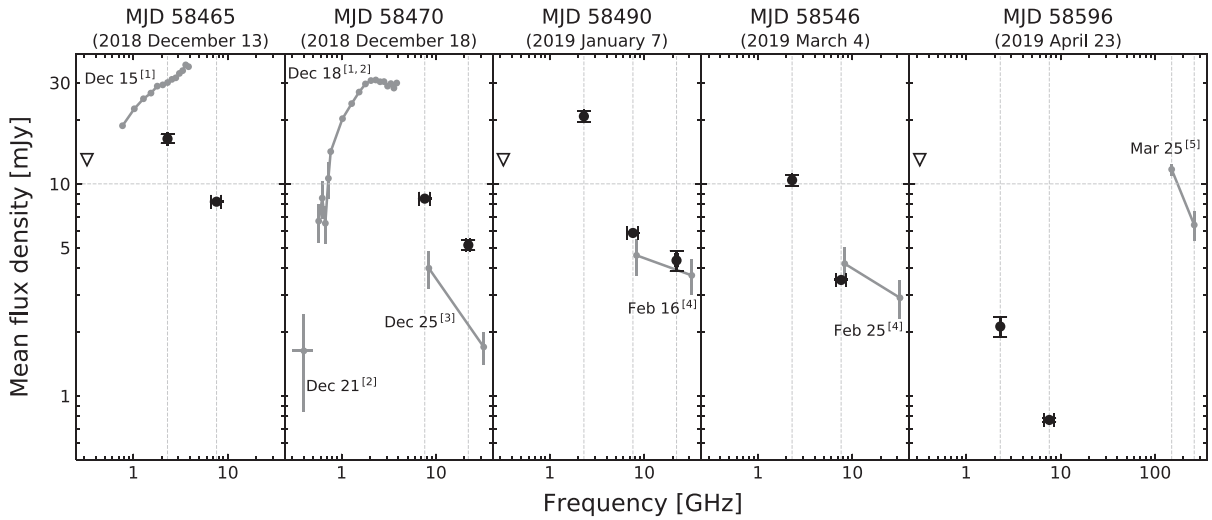

Fig. 5. Spectral variations of XTE J1810−197. Measured mean flux densities (converted to total intensity) at 2.3, 7.6, and 22 GHz are presented. For comparison, we added the flux densities obtained by [1] Dai et al. (2019), [2] Maan et al. (2019), [3] Pearlman et al. (2019), [4] Pearlman et al. (2020), and [5] Torne et al. (2020) using connected gray dots. Downwards pointing triangles indicate upper limits at 0.3 GHz.

and 260 GHz). In contrast to Maan et al. (2019) showing a monotonous positive spectral index at a broad low-frequency band of 0.3–4 GHz by combining their results with the results of Dai et al. (2019), the negative spectra at higher frequencies from our observations indicate that it is very difficult to explain the broad-band spectrum with a single power law, especially when we pay attention to the spectrum on MJD 58470 (2018 December 18).

In the frequency range up to ∼10 GHz, XTE J1810−197 shows a characteristic feature of a gigahertz-peaked spectrum (GPS). To verify the GPS appearance even with the daily variations, we estimate a degree of flux variation from the daily observations at 1.52 GHz made by Levin et al. (2019) (see the top panel of figure 4). The flux density has drastically decreased during the two local minima on MJDs 58466 and 58478; down to ∼−35% in two days for both troughs. Even though assuming at most 50% of daily flux changes randomly without a frequency-dependence, the flux density at 7.6 GHz is lower than the flux densities at 1.5–3 GHz. Hence, XTE J1810–197 would still possess the GPS feature with a peak frequency between 1.5 and 7.6 GHz. Moreover, the flux densities at adjacent frequencies would change similarly as seen in figure 4, thus the overall shape of the spectra is expected to be relatively stable.

Such a GPS feature has already been discussed for radio pulsars and other radio-bright magnetars. Among known radio pulsars, 11 or more GPS pulsars have been identified (Jankowski et al. 2018) and they may account for up to 10% of the pulsar population (Bates et al. 2013). They typically have peak frequencies around 1 GHz or smaller (Kijak et al. 2017). Two radio magnetars, 1E 1547.1−5408 and PSR J1622−4950, have shown apparent GPS shapes with peak frequencies of 5 GHz and 8.3 GHz, respectively (Kijak et al. 2013). The turn-over features can be attributed to the thermal free–free absorption of the pulsar radio emission in peculiar environments, such as supernova remnants, pulsar wind nebulae, or dense H II regions (Sieber 1973; Kijak et al. 2011). A radio magnetar located in the Galactic center, SGR J1745−2900, has also been suggested to be a GPS pulsar candidate, while no apparent increase in flux density at low frequency was detected (Lewandowski et al. 2015). Lewandowski et al. (2015) suggest the free–free absorption in the electron material ejected during a magnetar outburst could be responsible for the GPS and the spectral evolution with peak frequency shifting toward lower frequency. As for XTE J1810−197, we could imply a long-term shift of the GPS peak to the lower frequency from two results; (I) the decrease of the peak frequency in five days in the early spectra at 0.7–4 GHz (Dai et al. 2019) and (II) the steepening spectra at 2.3–7.6 GHz from our observations. To discuss further the free–free absorption model by materials from the magnetar outburst and thus explain the spectral variations of XTE J1810–197, short-cadence observations around peak frequencies are needed for coming outbursts.

XTE J1810−197 has a more complicated spectral transition at higher radio frequencies over 20 GHz; the negative spectrum extending to 22 GHz is expected to face a spectral upturn. Indeed, as marked in figure 5, Torne et al. (2020) detected a magnetar emission on MJD 58567 (2019 March 25) at 150 and 260 GHz whose mean flux densities [11.7(7) mJy and 6.4(10) mJy, respectively] are higher than our upper limit at 22 GHz on MJD 58529

(2019 February 15; 2.6 mJy). The higher-frequency intensities are even stronger than the intensity at 7.6 GHz obtained before and after their observation; the closest observation on MJD 58573 (2019 March 31) presents 0.90 ± 0.01 mJy at 7.6 GHz, suggesting that the spectrum would be inverted at over 22 GHz and has a second spectral peak between 22–150 GHz. Here we remark that the high-frequency peak is plausible, even allowing daily flux fluctuations up to 50%, as is confirmed for GPS. Thus we suggest XTE J1810−197 would have a bimodal spectrum in the frequency range of between 300 MHz and 250 GHz.

Double-peaked spectral features have also recently been discussed for two other radio magnetars, SGR J1745−2900 and PSR J1622−4950, indicating that the emission mechanism could be different at low- and high-frequency ranges (Chu et al. 2021). However, including for XTE J1810−197, it is necessary to note that only simultaneous wide-band observations would confirm their extraordinary spectral shapes. However, if true, they would be the first group with multiple spectral peaks in the radio band in the whole neutron star population. Although not all magnetar radio spectra have double-peaked features, this spectral hallmark could be intrinsic to radio magnetars, giving a new insight to the study of radio emissions from neutron stars in the wide frequency domain. For better constraints for magnetar emission models at different frequency ranges, tracing the timely variations of the double peaks would be highly required. Further multi-epoch broad-band observations toward radio-loud magnetars, therefore, would be necessary to investigate the origin and behavior of the double-peaked spectra.

4.2 Pulse width narrowing behavior

We showed the pulse width variations in subsection 3.2. During the second outburst, XTE J1810−197 shows the narrower average profile towards high frequency in the range of 2.3–22 GHz. This inverse frequency-dependency of the pulse width is one of the general features of plenty of ordinary pulsars (Pilia et al. 2016). A radius-to-frequency mapping (RFM; Cordes 1978) is usually used to describe the narrowing of pulse profiles. The RFM model postulates that higher radio frequency emission originates from lower altitudes of the neutron star, thus the pulse profile width would increase towards lower observing frequencies. Most of the average profiles of XTE J1810−197 at 2.3–22 GHz during our observing period have a single peak and we did not find a significant phase lag between pulse peaks at different frequencies with the same polarization information implying that the observed peak would be a core component when based on the RFM model. The model is, however, based on the dipole magnetic field structure and expects S-shaped polarization angle swings within the framework of a rotating vector model (RVM). The dramatic changes of the polarization position angles of radio magnetars inhibit the application of a classical RVM to magnetars (e.g., Kramer et al. 2007). Although the RFM model might not be plausible for the cases of radio magnetars, the profile-narrowing trend of XTE J1810−197 could give a hint for some form of link between magnetar radio emission and standard pulsar emission in terms of magnetospheric structures. However, the pulse width variations of radio magnetars during an outburst, even only for XTE J1810−197, are yet poorly understood, hence high-sensitive long-term investigations on the variability in radio profiles of magnetars are required for each radio outburst.

A recent study of pulse widths for ordinary pulsars, however, estimated that more than 20% of ordinary pulsars show positive correlations between pulse width and observing frequency, implying a diversity in the energy spectrum distribution across the emission regions of neutron stars (Chen & Wang 2014). While most radio magnetars have rather stable or slightly narrowing pulse width over frequency (e.g., Wharton et al. 2019; Lower et al. 2020), PSR J1622–4950 showed not only profile narrowing from 1.4 GHz to 6.6 GHz, but also slight profile broadening at 17 GHz (Levin et al. 2012). When it comes to radio-loud magnetars, only a few atypical properties are known to be commonly seen, hindering an integrated understanding of the radio-emitting magnetars altogether. Searching the additional common features of magnetar radio pulsations would enable a comprehensive understanding of them. We, therefore, stress the necessity of investigations into the frequency-dependence of pulse widths of radio magnetars through simultaneous multi-frequency observations, and this would enable a better understanding of the magnetospheric geometry of magnetars. We, in addition, note that in the long-term, radio magnetars can provide crucial samples for studying the ultra wideband frequency dependency of pulse width with the benefit of their flat spectra.

5 Summary and conclusion

We conducted an analysis of the simultaneous observations of the radio-loud magnetar XTE J1810−197 with radio telescopes in Japan at 0.3, 2.3, 6.9, 8.4, and 22 GHz. Our observations were organized for six months during the revived radio outburst detected in 2018 December. Significant pulsed emissions were detected at the frequency range of 2.3–22 GHz and the radio pulsations generally became fainter during our observations.

By employing the timing solutions for the early phase of this outburst from the literature, we found that the change of the spin frequency derivative has continuously weakened since the radio outburst. We also report that the duty cycle of the magnetar during this outburst is $\sim$5%, which is analogous to its previous outburst and a number of ordinary pulsars. The pulse widths tend to become narrower as the observing frequency becomes higher.

We obtained the negative spectra in 2.3–22 GHz with an average spectral index of -0.85 ± 0.14 at 2.3–8.7 GHz. By combining this with the flux densities at lower and higher frequencies from the literature, we suggest that XTE J1810−197 would have a bimodal spectrum with a GPS feature at frequencies under 7.6 GHz and a second peak at over 22 GHz. Considering that the magnetar radio emission is highly variable, we put special emphasis on the importance of long-term simultaneous broad-band observations of magnetar radio outbursts to understand the origin and emission mechanisms of magnetar radio pulsations.

Acknowledgments

We thank all staff of Mizusawa VLBI Observatory of NAOJ. We are grateful to Katsunori Shibata for providing information for VERA data reduction. Observations at the Hitachi 32 m telescope are supported by the inter-university collaborative project "Japanese VLBI Network" of NAOJ. This work is supported by JSPS/MEXT KAKENHI grant numbers 17H01116 (M.H.), 18H01245 (S.K.), 18H01246 (H.M., S.K., T.T.), 19K14712, and 21H01078 (S.K.).

References

Anderson, G. E., et al. 2012, ApJ, 751, 53
Bates, S. D., Lorimer, D. R., & Verbiest, J. P. W. 2013, MNRAS, 431, 1352
Borghese, A., et al. 2021, MNRAS, 504, 5244
Camilo, F., et al. 2007a, ApJ, 663, 497
Camilo, F., et al. 2007b, ApJ, 669, 561
Camilo, F., et al. 2016, ApJ, 820, 110
Camilo, F., Ransom, S. M., Halpern, J. P., Reynolds, J., Helfand, D. J., Zimmerman, N., & Sarkissian, J. 2006, Nature, 442, 892
Camilo, F., Reynolds, J., Johnston, S., Halpern, J. P., & Ransom, S. M. 2008, ApJ, 679, 681
Champion, D., et al. 2020, MNRAS, 498, 6044
Chen, J. L., & Wang, H. G. 2014, ApJS, 215, 11
Chu, C.-Y., Ng, C. Y., Kong, A. K. H., & Chang, H.-K. 2021, MNRAS, 503, 1214
Cordes, J. M. 1978, ApJ, 222, 1006
Dai, S., et al. 2019, ApJ, 874, L14
Gotthelf, E. V., et al. 2019, ApJ, 874, L25
Halpern, J. P., Gotthelf, E. V., Becker, R. H., Helfand, D. J., & White, R. L. 2005, ApJ, 632, L29
Hankins, T. H., & Rickett, B. J. 1975, Methods Comput. Phys., 14, 55
Hobbs, G. B., Edwards, R. T., & Manchester, R. N. 2006, MNRAS, 369, 655
Ibrahim, A. I., et al. 2004, ApJ, 609, L21
Iwai, K., Tsuchiya, F., Morioka, A., & Misawa, H. 2012, Sol. Phys., 277, 447
Jankowski, F., van Straten, W., Keane, E. F., Bailes, M., Barr, E. D., Johnston, S., & Kerr, M. 2018, MNRAS, 473, 4436
Johnston, S., et al. 2020, MNRAS, 493, 3608
Kijak, J., Basu, R., Lewandowski, W., Rożko, K., & Dembska, M. 2017, ApJ, 840, 108
Kijak, J., Lewandowski, W., Maron, O., Gupta, Y., & Jessner, A. 2011, A&A, 531, A16
Kijak, J., Tarczewski, L., Lewandowski, W., & Melikidze, G. 2013, ApJ, 772, 29
Kramer, M., Stappers, B. W., Jessner, A., Lyne, A. G., & Jordan, C. A. 2007, MNRAS, 377, 107
Lazaridis, K., Jessner, A., Kramer, M., Stappers, B. W., Lyne, A. G., Jordan, C. A., Serylak, M., & Zensus, J. A. 2008, MNRAS, 390, 839
Levin, L., et al. 2010, ApJ, 721, L33
Levin, L., et al. 2012, MNRAS, 422, 2489
Levin, L., et al. 2019, MNRAS, 488, 5251
Lewandowski, W., Rożko, K., Kijak, J., & Melikidze, G. I. 2015, ApJ, 808, 18
Lorimer, D. R., & Kramer, M. 2012, Handbook of Pulsar Astronomy (Cambridge: Cambridge University Press)
Lower, M. E., Shannon, R. M., Johnston, S., & Bailes, M. 2020, ApJ, 896, L37
Lyne, A., Levin, L., Stappers, B., Mickaliger, M., Desvignes, G., & Kramer, M. 2018, The Astronomer's Telegram, 12284, 1
Maan, Y., Joshi, B. C., Surnis, M. P., Bagchi, M., & Manoharan, P. K. 2019, ApJ, 882, L9
Maciesiak, K., Gil, J., & Ribeiro, V. A. R. M. 2011, MNRAS, 414, 1314
Majid, W. A., Pearlman, A. B., Prince, T. A., Naudet, C. J., & Bansal, K. 2020, The Astronomer's Telegram, 13898, 1
Maron, O., Kijak, J., Kramer, M., & Wielebinski, R. 2000, A&AS, 147, 195
Mikami, R., et al. 2016, ApJ, 832, 212
Olausen, S. A., & Kaspi, V. M. 2014, ApJS, 212, 6
Pearlman, A. B., et al. 2020, arXiv:2005.08410
Pearlman, A. B., Majid, W. A., & Prince, T. A. 2019, Adv. Astron., 2019, 6325183
Pennucci, T. T., et al. 2015, ApJ, 808, 81
Pilia, M., et al. 2016, A&A, 586, A92
Pintore, F., et al. 2016, MNRAS, 458, 2088
Sieber, W. 1973, A&A, 28, 237
Thompson, C., & Duncan, R. C. 1993, ApJ, 408, 194
Torne, P., et al. 2015, MNRAS, 451, L50
Torne, P., et al. 2020, A&A, 640, L2
Tsuchiya, F., Misawa, H., Imai, K., Morioka, A., & Kondo, T. 2010, in Advances in Geosciences, Vol. 19, ed. A. Bhardwaj (Singapore: World Scientific), 601
VERA Collaboration,2020, PASJ, 72, 50
Wharton, R. S., et al. 2019, ApJ, 875, 143
Yonekura, Y., et al. 2016, PASJ, 68, 74